# Underwater Image Enhancement by Wavelength Compensation and Dehazing

John Y. Chiang and Ying-Ching Chen

*Abstract*—Light scattering and color change are two major sources of distortion for underwater photography. Light scattering is caused by light incident on objects reflected and deflected multiple times by particles present in the water before reaching the camera. This in turn lowers the visibility and contrast of the image captured. Color change corresponds to the varying degrees of attenuation encountered by light traveling in the water with different wavelengths, rendering ambient underwater environments dominated by a bluish tone. No existing underwater processing techniques can handle light scattering and color change distortions suffered by underwater images, and the possible presence of artificial lighting simultaneously. This paper proposes a novel systematic approach to enhance underwater images by a dehazing algorithm, to compensate the attenuation discrepancy along the propagation path, and to take the influence of the possible presence of an artifical light source into consideration. Once the depth map, i.e., distances between the objects and the camera, is estimated, the foreground and background within a scene are segmented. The light intensities of foreground and background are compared to determine whether an artificial light source is employed during the image capturing process. After compensating the effect of artifical light, the haze phenomenon and discrepancy in wavelength attenuation along the underwater propagation path to camera are corrected. Next, the water depth in the image scene is estimated according to the residual energy ratios of different color channels existing in the background light. Based on the amount of attenuation corresponding to each light wavelength, color change compensation is conducted to restore color balance. The performance of the proposed algorithm for wavelength compensation and image dehazing (WCID) is evaluated both objectively and subjectively by utilizing ground-truth color patches and video downloaded from the Youtube website. Both results demonstrate that images with significantly enhanced visibility and superior color fidelity are obtained by the WCID proposed.

*Index Terms*—Color change, image dehazing, light scattering, underwater image, wavelength compensation.

## I. INTRODUCTION

ACQUIRING clear images in underwater environments is an important issue in ocean engineering [1], [2]. The quality of underwater images plays a pivotal role in scientific missions such as monitoring sea life, taking census of populations, and assessing geological or biological environments. Capturing images underwater is challenging, mostly due to

Fig. 1. Hazing and bluish effects caused by light scattering and color change in underwater images. This image is part of an underwater footage on the Youtube website filmed by the Bubble Vision Company.

haze caused by light that is reflected from a surface and is deflected and scattered by water particles, and color change due to varying degrees of light attenuation for different wavelengths [3]–[5]. Light scattering and color change result in contrast loss and color deviation in images acquired underwater. For example, in Fig. 1, the haze in the school of Carangid, the diver, and the reef at the back is attributed to light scattering, whereas color change is the reason for the bluish tone appearing in the brown coral reef at the bottom and the yellow fish in the upper-right corner.

Haze is caused by suspended particles such as sand, minerals, and plankton that exist in lakes, oceans, and rivers. As light reflected from objects propagates toward the camera, a portion of the light meets these suspended particles. This in turn absorbs and scatters the light beam, as illustrated in Fig. 2. In the absence of blackbody radiation [6], the multiscattering process along the course of propagation further disperses the beam into homogeneous background light.

Conventionally, the processing of underwater images focuses solely on compensating either light scattering or color change distortion. Techniques targeting on removal of light scattering distortion include exploiting the polarization effects to compensate for visibility degradation [7], using image dehazing to restore the clarity of the underwater images [8], and combining point spread functions and a modulation transfer function to reduce the blurring effect [9]. Although the aforementioned approaches can enhance scene contrast and increase visibility, distortion caused by the disparity in wavelength attenuation, i.e., color change, remains intact. On the other hand, color-change correction techniques estimate underwater environmental parameters by performing color registration with consideration of
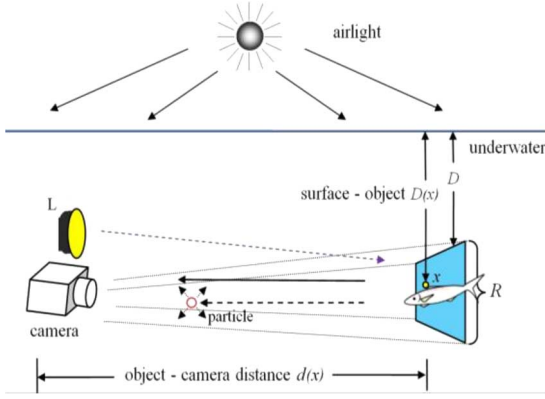
Fig. 2. Natural light enters from air to an underwater scene point $x$. The light reflected propagates distance $d(x)$ to the camera. The radiance perceived by the camera is the sum of two components: the background light formed by multiscattering and the direct transmission of reflected light.
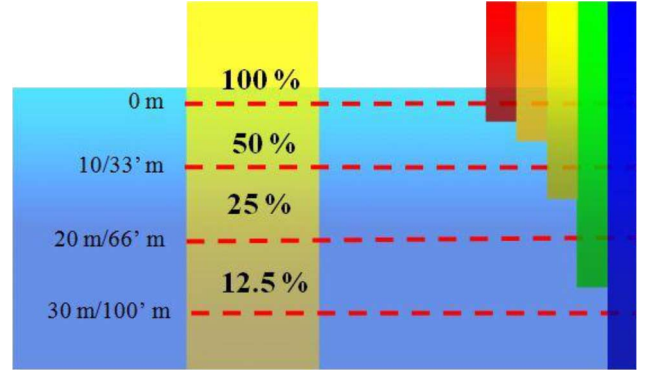


Fig. 3. Different wavelengths of light are attenuated at different rates in water. The blue color travels the longest in the water due to its shortest wavelength. This is the reason that underwater images are dominated by blue color.

light attenuation [10], employing histogram equalization in both RGB and HSI color spaces to balance the luminance distributions of color [11], and dynamically mixing the illumination of an object in a distance-dependent way by using a controllable multicolor light source to compensate color loss [12]. Despite the improved color balance, these methods are ineffective in removing the image blurriness caused by light scattering. A systematic approach is needed to take all the factors concerning light scattering, color change, and possible presence of artificial light source into consideration.

The algorithm for wavelength compensation and image dehazing (WCID) proposed in this paper combines techniques of WCID to remove distortions caused by light scattering and color change. Dark-channel prior [13], an existing scene-depth derivation method, is used first to estimate the distances of the scene objects to the camera. The low intensities in the dark channel are mainly due to three factors: 1) shadows, e.g., the shadows of creatures, plankton, plants, or rocks in seabed images; 2) colorful objects or surfaces, e.g., green plants, red or yellow sands, and colorful rocks/minerals, deficient in certain color channels; and 3) dark objects or surfaces, e.g., dark creatures and stone [8]. Based on the depth map derived, the foreground and background areas within the image are segmented. The light intensities of foreground and background are then compared to determine whether an artificial light source is employed during the image acquiring process. If an artificial light source is detected, the luminance introduced by the auxiliary lighting is removed from the foreground area to avoid overcompensation in the stages followed. Next, the dehazing algorithm and wavelength compensation are utilized to remove the haze effect and color change along the underwater propagation path to the camera. The residual energy ratio among different color channels in the background light is employed to estimate the water depth within an underwater scene. Energy compensation for each color channel is carried out subsequently to adjust the bluish tone to a natural color. With WCID, expensive optical instruments or stereo image pairs are no longer required. WCID can effectively enhance visibility and restore the color balance of underwater images, rendering high visual clarity and color fidelity.

## A. Underwater Model

The background light in an underwater image can be used to approximate the true in-scattering term in the full radiative transport equation to achieve the following simplified hazy image formation model [14], [15]:

$$I_\lambda(x) = J_\lambda(x) \cdot t_\lambda(x) + (1 - t_\lambda(x)) \cdot B_\lambda, \lambda \in \{\text{red, green, blue}\} \quad (1)$$

where $x$ is a point in the underwater scene, $I_\lambda(x)$ is the image captured by the camera, $J_\lambda(x)$ is the scene radiance at point $x$, $t_\lambda(x)$ is the residual energy ratio of $J_\lambda(x)$ after reflecting from point $x$ in the underwater scene and reaching the camera, $B_\lambda$ is the homogeneous background light, and $\lambda$ is the light wavelength. Note that the residual energy ratio $t_\lambda(x)$ is a function of both wavelength $\lambda$ and the object–camera distance $d(x)$. $t_\lambda(x)$ summarizes the overall effects for both light scattering and color change suffered by light with wavelength $\lambda$ traveling the underwater distance $d(x)$. The direct attenuation term $J_\lambda(x)t_\lambda(x)$ describes the decay of scene radiance in the water [16]. The residual energy ratio $t_\lambda(x)$ can be represented alternatively as the energy of a light beam with wavelength $\lambda$ before and after traveling distance $d(x)$ within the water $E_\lambda^{\text{initial}}(x)$ and $E_\lambda^{\text{residual}}(x)$, respectively, as follows:

$$t_\lambda(x) = \frac{E_\lambda^{\text{residual}}(x)}{E_\lambda^{\text{initial}}(x)} = 10^{-\beta(\lambda)d(x)} = \text{Nrer}(\lambda)^{d(x)} \quad (2)$$

where the normalized residual energy ratio $\text{Nrer}(\lambda)$ corresponds to the ratio of residual to initial energy for every unit of distance propagated and $\beta(\lambda)$ is the medium extinction coefficient [15]. The normalized residual energy ratio $\text{Nrer}(\lambda)$ depends on the light wavelength transmitted [17], as illustrated in Fig. 3, where red light possesses longer wavelength and lower frequency and thereby attenuates faster than the blue counterpart. This results in the bluish tone prevalent in underwater images [18]. Other than the wavelength of light transmitted, the normalized residual energy ratio $\text{Nrer}(\lambda)$ is also affected by water salinity and concentration of phytoplankton [17]. In light of this observation, oceanic water is further classified into three categories. Type-I waters represent extremely clear oceanic waters. Most clear coastal waters with a higher level of attenuation

Underwater images acquired

Haze-free and color-corrected underwater images

Derivation of *d(x)* by dark-channel prior & image matting

Depth map

Segmentation of foreground and background

Artificial light source *L*?

Compensation of color change along the course of propagation *D* through *D+R*

Estimation of scene range from depth *D* through *D+R*

Compensation of light scattering & color change along the path *d(x)*

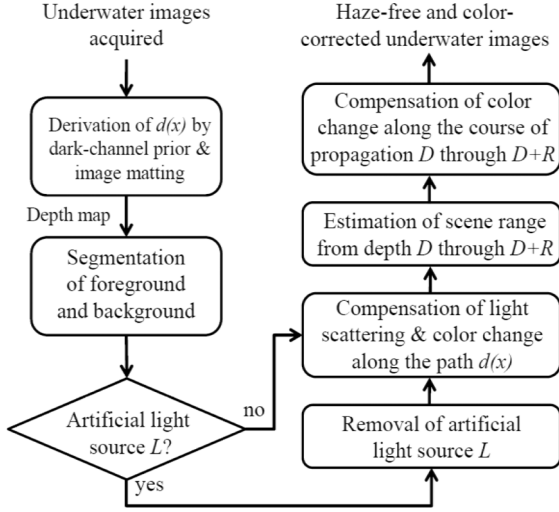Removal of artificial light source *L*

no

yes

Fig. 4.  Flowchart of the WCID algorithm proposed.

belong to the Type-II class. Turbid upwelling coastal waters are listed as Type III. Water types I, II, and III roughly correspond to oligo-, meso-, and eutrophic waters [19]. For every meter of ocean type I that a light beam passes through, the values of normalized residual energy ratio Nrer($\lambda$) in red (700 $\mu$m) light, green (520 $\mu$m) light, and blue (440 $\mu$m) light are 82%, 95%, and 97.5%, respectively. Based on the water type considered, the normalized residual energy ratio Nrer($\lambda$) can be adjusted based on that of Ocean Type I as follows:

$$\text{Nrer}(\lambda) = \begin{cases} 0.8 \sim 0.85 & \text{if } \lambda = 650 \sim 750 \ \mu\text{m(red)}, \\ 0.93 \sim 0.97 & \text{if } \lambda = 490 \sim 550 \ \mu\text{m(green)}, \\ 0.95 \sim 0.99 & \text{if } \lambda = 400 \sim 490 \ \mu\text{m(blue)}. \end{cases} \tag{3}$$

## II. UNDERWATER IMAGE FORMATION MODEL

The proposed WCID algorithm proceeds in a direction inverse to the underwater image formation path discussed above, as depicted in Fig. 4. First, consider the possible presence and influence of the artificial light source $L$. Next, remove the light scattering and color change that occurred along the course of propagation $d(x)$ from the object to the camera. Finally, compensate the disparities of wavelength attenuation for traversing the water depth $D$ to the top of the image and fine-tune the energy loss by deriving a more precise depth value for every point within an image.

Fig. 2 illustrates an underwater image formation model. Homogeneous skylight entering above into the water is the major source of illumination in an underwater environment. Incident light traverses from the surface of water reaching the image scene, covering a range from depth $D$ through $D + R$, where $R$ corresponds to the image depth range. During the course of propagation, light with different wavelengths is subjected to varying degrees of attenuation. The color change of ambient lighting makes the underwater environment tinted with a bluish hue. As airlight $A$ incident from air to the water reaches the underwater scene point $x$ with depth $D(x)$, i.e., $D < D(x) <$

$D + R$, the amount of residual light $W(x)$ formed after wavelength attenuation can be formulated according to the energy attenuation model in (2) as follows:

$$E_\lambda^W(x) = E_\lambda^A(x) \cdot \text{Nrer}(\lambda)^{D(x)}, \lambda \in \{\text{red, green, blue}\}. \tag{4}$$

At point $x$, the light reflected again travels distance $d(x)$ to the camera forming pixel $I_\lambda(x)$, $\lambda \in \{\text{red, green, blue}\}$. Along this underwater object–camera path, two phenomena occur, i.e., light scattering and color change. Note that color change occurs not only along the surface–object propagation path but also along the object–camera route. Light $J_\lambda(x)$ emanated from point $x$ is equal to the amount of illuminating ambient light $E_\lambda^w(x)$ reflected, i.e., $E_\lambda^w(x) \cdot \rho_\lambda(x) = E_\lambda^A(x) \cdot \text{Nrer}(\lambda)^{D(x)} \cdot \rho_\lambda(x)$, where $\rho_\lambda(x)$ is the reflectivity of point $x$ for light with wavelength $\lambda$. By following the image formation model in a hazy environment in (1), the image $I_\lambda(x)$ formed at the camera can be formulated as follows:

$$I_\lambda(x) = \left( E_\lambda^A(x) \cdot \text{Nrer}(\lambda)^{D(x)} \cdot \rho_\lambda(x) \right) \cdot t_\lambda(x) + (1 - t_\lambda(x)) \\ \cdot B_\lambda, \lambda \in \{\text{red, green, blue}\} \tag{5}$$

where the background light $B_\lambda$ represents the part of the object reflected light $J_\lambda$ and ambient light $E_\lambda^w$ scattered toward the camera by particles in the water.

The background light $B_\lambda$ increases as the object is placed farther away from the camera [13], [20]–[23]. Alternatively, the residual energy ratio $t_\lambda(x)$ in the above equation can be represented in terms of normalized residual energy ratio Nrer($\lambda$) using (2) as follows:

$$I_\lambda(x) = \left( E_\lambda^A(x) \cdot \text{Nrer}(\lambda)^{D(x)} \cdot \rho_\lambda(x) \right) \cdot \text{Nrer}(\lambda)^{d(x)} \\ + \left( 1 - \text{Nrer}(\lambda)^{d(x)} \right) \cdot B_\lambda, \lambda \in \{\text{red, green, blue}\}. \tag{6}$$

Equation (6) incorporates light scattering during the course of propagation from object to the camera $d(x)$, and the wavelength attenuation along both the surface–object path $D(x)$ and object–camera route $d(x)$, Once the scene depth, i.e., object–camera distance $d(x)$, is known through the dark-channel prior, the value of residual energy ratio $\text{Nrer}(\lambda)^{d(x)}$ after wavelength attenuation can be calculated; thus, the direct attenuation term $E_\lambda^A(x) \cdot \text{Nrer}(\lambda)^{D(x)} \cdot \rho_\lambda(x)$ is derivable through a dehazing procedure. The surface–object distance $D(x)$ is calculated by comparing the residual energy ratio of different color channels. Given the water depth $D(x)$, the amount of reflecting light $E_\lambda^A(x) \cdot \rho_\lambda(x)$, i.e., free of light scattering and color change, from point $x$ illuminated by airlight is determined.

Moreover, the artificial light source $L$ is often provided to overcome insufficient lighting commonly encountered in an underwater photographic environment. The luminance contributed by the artificial light source has to be removed before the dehazing and wavelength compensation operations to avoid overcompensation. When the artificial light source $L$ is detected, the light emitted $E_\lambda^L$ has first to travel distance $d(x)$ before reaching point $x$. The residual energy after the course of propagation is $E_\lambda^L \cdot \text{Nrer}(\lambda)^{d(x)}$. The total amount of light impinges on point $x$ is therefore the summation of ambient lighting $E_\lambda^w(x)$ and the attenuated artificial light $E_\lambda^L \cdot \text{Nrer}(\lambda)^{d(x)}$. The total amount of

incident light $E_\lambda^A(x) \cdot \mathrm{Nrer}(\lambda)^{D(x)} + E_\lambda^L \cdot \mathrm{Nrer}(\lambda)^{d(x)}$ is reflected with reflectivity $\rho_\lambda(x)$ and bounces back distance $d(x)$ before reaching the camera. During both forward and backward courses of propagation pertinent to $d(x)$, color change occurs. Accordingly, (6) can be further modified as the hazy image formation equation

$$I_\lambda(x) = \Big( \big( \overbrace{E_\lambda^A(x) \cdot \mathrm{Nrer}(\lambda)^{D(x)}}^{\text{airlight color change along } D(x)} + \overbrace{E_\lambda^L \cdot \mathrm{Nrer}(\lambda)^{d(x)}}^{\substack{\text{artificial lighting color} \\ \text{change from light} \\ \text{source to } x \text{ along } d(x)}} \big) \cdot \rho_\lambda(x) \Big) \cdot \mathrm{Nrer}(\lambda)^{d(x)} + \overbrace{(1 - \mathrm{Nrer}(\lambda)^{d(x)}) \cdot B_\lambda}^{\text{source of haze}},$$
$$\underbrace{\phantom{\big( E_\lambda^A \cdot \mathrm{Nrer} + E \big)}}_{\text{total amount of incident light at } x}$$
$$\underbrace{\phantom{\big( \big( E_\lambda^A \cdot \mathrm{Nrer} + E \big) \cdot \rho \big) \cdot \mathrm{Nrer}}}_{\text{reflected light color change from } x \text{ to camera along } d(x)} \qquad \lambda \in \{red, green, blue\}.$$

(7)

The underwater image formation model in (7) takes the hazing effect, wavelength attenuation, and artificial lighting into consideration. Given the signal $I_\lambda(x)$ perceived, our goal is to remove the influences of artificial lighting, hazing, and color change along the object–camera path, and color change suffered from water surface to object, as outlined in the previous paragraph. The following subsections will discuss the steps for the estimation of the object–camera distance $d(x)$, the artificial light source $L$, the water depth $D$, the depth range $R$, and the corresponding procedures for dehazing and energy compensation.

### A. Distance Between the Camera and the Object: $d(x)$

The common approach for estimating the depth of objects within a scene, i.e., depth map, often requires two images for parallax [20]. In a hazy environment, haze increases with distance; therefore, haze itself can be a useful depth clue for scene understanding. Consequently, evaluating the concentration of haze in a single image is sufficient to predict the distance $d(x)$ between the object in the scene and the camera [21]. The dark-channel prior [8], which is an existing scene-depth derivation method, is based on the observation that, in most of the non-background light patches $\Omega(x)$, where $x \in \Omega(x)$, on a haze-free underwater image, at least one color channel has a very low intensity at some pixels. In other words, the minimum intensity in such a patch should have a very low value, i.e., a dark channel. Note that the low intensity observed through the dark channel is a consequence of low reflectivity $\rho_\lambda(x)$ existing in certain color channels. No pixels with a very low value can be found in the local patch $\Omega(x)$, which implies the existence of haze. The concentration of haze in a local patch can then be quantified by dark-channel prior. This in turn provides the object–camera distance $d(x)$ [13].

As formulated in (7), light $J_\lambda(x)$ reflected from point $x$ is

$$J_\lambda(x) = \Big( E_\lambda^A(x) \cdot \mathrm{Nrer}(\lambda)^{D(x)} + E_\lambda^L \cdot \mathrm{Nrer}(\lambda)^{d(x)} \Big)$$
$$\cdot \rho_\lambda(x), \lambda \in \{red, green, blue\}. \quad (8)$$

We define the dark channel $J_{\mathrm{dark}}(x)$ for the underwater image $J_\lambda(x)$ as

$$J_{\mathrm{dark}}(x) = \min_\lambda \min_{y \in \Omega(x)} J_\lambda(y), \lambda \in \{red, green, blue\}. \quad (9)$$

If point $x$ belongs to a part of the foreground object, the value of the dark channel is very small, i.e., $J_{\mathrm{dark}}(x) \approx 0$. Taking the min operation in the local patch $\Omega(x)$ on the hazy image $I_\lambda(x)$ in (7), we have

$$\min_{y \in \Omega(x)} (I_\lambda(y)) = \min_{y \in \Omega(x)} \Big\{ J_\lambda(y) \cdot \mathrm{Nrer}(\lambda)^{d(y)}$$
$$+ \Big( 1 - \mathrm{Nrer}(\lambda)^{d(y)} \Big) \cdot B_\lambda \Big\}, \lambda \in \{red, green, blue\}. \quad (10)$$

Since $B_\lambda$ is the homogeneous background light and the residual energy ratio $\mathrm{Nrer}(\lambda)^{d(y)}$ on the small local patch $\Omega(x)$ surrounding point $x$ is essentially a constant $\mathrm{Nrer}(\lambda)^{d(x)}$ [21], the min value on the second term of (10) can be subsequently removed as

$$\min_{y \in \Omega(x)} (I_\lambda(y)) = \min_{y \in \Omega(x)} J_\lambda(y) \cdot \mathrm{Nrer}(\lambda)^{d(x)}$$
$$+ \Big( 1 - \mathrm{Nrer}(\lambda)^{d(x)} \Big) \cdot B_\lambda, \lambda \in \{red, green, blue\}. \quad (11)$$

We rearrange the above equation and perform one more min operation among all three color channels as follows:

$$\min_\lambda \left\{ \frac{\min_{y \in \Omega(x)} (I_\lambda(x))}{B_\lambda} \right\}$$
$$= \min_\lambda \left\{ \frac{\min_{y \in \Omega(x)} J_\lambda(y)}{B_\lambda} \cdot \mathrm{Nrer}(\lambda)^{d(x)} \right\}$$
$$+ \min_\lambda \Big( 1 - \mathrm{Nrer}(\lambda)^{d(x)} \Big), \lambda \in \{red, green, blue\}.$$

(12)

The first term on (12) can be shown to satisfy the following inequality (refer to Appendix I for details):

$$0 < \min_\lambda \left\{ \frac{\min_{y \in \Omega(x)} (J_\lambda(y))}{B_\lambda} \cdot \mathrm{Nrer}(\lambda)^{d(x)} \right\}$$
$$\leq \frac{\min_\lambda \Big( \min_{y \in \Omega(x)} J_\lambda(y) \Big) \cdot \min_\lambda \big( \mathrm{Nrer}(\lambda)^{d(x)} \big)}{\min_\lambda (B_\lambda)}. \quad (13)$$

The first term in the numerator of (13) is equal to the dark channel $J_{\mathrm{dark}}(x)$ defined in (9) and is very close to zero. Therefore, (12) can be rewritten as

$$\min_\lambda \Big( \mathrm{Nrer}(\lambda)^{d(x)} \Big) = 1 - \min_\lambda \left\{ \frac{\min_{y \in \Omega(x)} (I_\lambda(y))}{B_\lambda} \right\},$$
$$\lambda \in \{red, green, blue\}. \quad (14)$$

Among all color channels, $\mathrm{Nrer}(red)$ possesses the lowest residual value. This indicates that $\min_\lambda (\mathrm{Nrer}(\lambda)^{d(x)})$, $\lambda \in \{red, green, blue\}$ is simply equal to $\mathrm{Nrer}(red)$. The background light $B_\lambda$ is usually assumed to be the pixel intensity with the highest brightness value in an image [20]. However, this simple assumption often renders erroneous results due to the presence of self-luminous organisms or an extremely smooth surface, e.g., a white fish. In order to increase the detection robustness of background light, a min operation is first performed in every local patch $\Omega(x)$ of all pixels $x$ in a
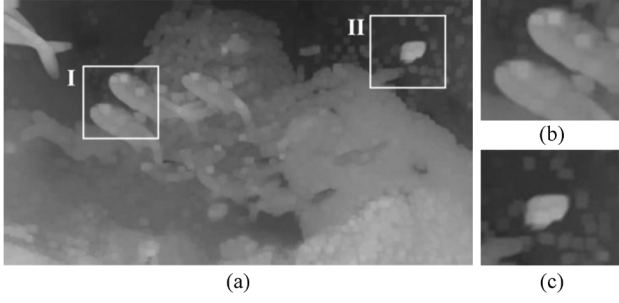
Fig. 5. (a) Depth map obtained by estimating $d(x)$, which is the distance between the object and the camera using dark-channel prior. Blowups of (b) Frame I and (c) Frame II. Visible mosaic artifacts are observed due to the block-based operation of dark-channel prior.
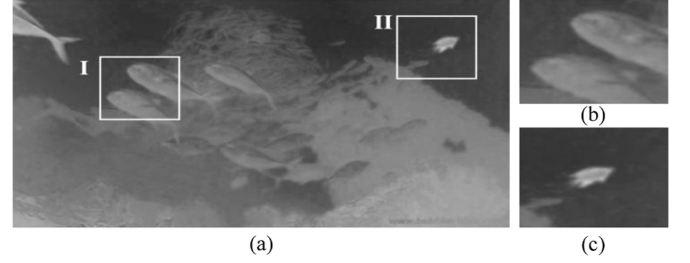


Fig. 6. (a) Depth map obtained after refining with image matting. Blowups of (b) Frame I and (c) Frame II. When compared with Fig. 5(b) and (c), the depth map after refinement reduces the mosaic effect and captures the contours of objects more accurately.

hazy image $I$. The brightest pixel value among all local minima corresponds to the background light $B_\lambda$ as follows:

$$B_\lambda = \max_{x \in I} \min_{y \in \Omega(x)} I_\lambda(y), \quad \lambda \in \{\text{red, green, blue}\}. \quad (15)$$

Given the values of $I_\lambda(y)$, $B_\lambda$, and Nrer(red), distance $d(x)$ between point $x$ on an object and the camera can be determined. The depth map of Fig. 1 is shown in Fig. 5(a).

Block-based dark-channel prior will inevitably introduce a mosaic artifact and produce a less accurate depth map, as shown in Fig. 5(b) and (c). By imposing a locally linear assumption for foreground and background colors and applying image matting to repartition the depth map, the mosaic effect is reduced, and object contours can be identified more precisely [13], [22]. Applying image matting to the underwater depth map derived by the general dark-channel methodology is a novel approach. We denote the depth map of Fig. 5(a) as $\mathbf{d}_{\text{coarse}}$. The depth map after refinement $\mathbf{d}_{\text{refined}}$ can be formulated as

$$(\mathbf{L} + \Lambda\mathbf{U})\mathbf{d}_{\text{refined}} = \Lambda\mathbf{d}_{\text{coarse}} \quad (16)$$

where $\mathbf{U}$ is a unit matrix, $\Lambda$ is a regularization coefficient, and $L$ represents the matting Laplacian matrix as follows:

$$\mathbf{L}(i,j) = \sum_{x(i,j) \in w_x} \left( \delta_{ij} - \frac{1}{|w_x|} \right.$$
$$\left. \times \left( 1 + (I_i - \mu_x)^T \left( \sum_x + \frac{\varepsilon}{|w_x|} U \right)^{-1} (I_j - \mu_x) \right) \right) \quad (17)$$

where $I$ represents the original image, the coordinates of pixel $x$ are $(i,j)$, $\delta_{ij}$ is the Kronecker delta, $\Sigma_x$ is the color covariance of a small area $w_x$, $\mu_x$ is the mean color value of $w_x$, and $\varepsilon$ is a regularization coefficient. Fig. 6 shows the depth map after applying image matting to remove mosaic distortion.

### B. Removal of the Artificial Light Source $L$

Artificial light sources are often supplemented to avoid insufficient lighting commonly encountered in an underwater photographic environment, as shown in Fig. 7. If an artificial light source $L$ is employed during the image capturing process, the luminance contributed by $L$ must be deducted first to avoid



Fig. 7. Illuminated by an artificial light source, the intensity of the foreground appears brighter than that of the background.



Fig. 8. When the luminance contributed by an artificial light source is not deducted first, an overexposed image will be obtained after the compensation stages followed.

overcompensation for the stages followed, as illustrated in Fig. 8. Modeling, detecting, and compensating the presence of an artificial light source are novel to the processing of underwater images. The existence of an artificial light source can be determined by comparing the difference between the mean luminance of the foreground and the background. In an underwater image without artificial lighting, the dominant source of light originates from the airlight above the water surface. The underwater background corresponds to light transmitted without being absorbed and reflected by objects and is therefore the brighter part of the image. Higher mean luminance in the foreground of an image than that in the background indicates the existence of a supplementary light source. The foreground

and the background of an image can be segmented based on the depth map derived earlier as follows:

$$\text{area - type}(x) = \begin{cases} \text{foreground} & \text{if } d(x) > \sigma \\ \text{background} & \text{if } d(x) \leq \sigma \end{cases} \quad (18)$$

where $d(x)$ is the distance between the object and the camera, whereas $\sigma$ is a threshold.

Upon detection of the presence of an artificial lighting, the added luminance introduced by the artificial light source has to be removed. The influence of an artificial lighting perceived by the camera is a function of the amount of luminance contributed by the light source and surface reflectance of objects. Since a point light source emanates spherically, the amount of the luminance supplied is inversely proportional to the square of the distance between the object and the light source. The closer the object, the stronger the intensity of the artificial light source, and vice versa. As discussed earlier, the light $J_\lambda(x) = (E_\lambda^A(x) \cdot \text{Nrer}(\lambda)^{D(x)} + E_\lambda^L \cdot \text{Nrer}(\lambda)^{d(x)}) \cdot \rho_\lambda(x)$ reflected from point $x$ is equal to the product of reflectivity $\rho_\lambda(x)$ times the summation of the ambient lighting $E_\lambda^A(x) \cdot \text{Nrer}(\lambda)^{D(x)}$ and the attenuated artificial light $E_\lambda^L \cdot \text{Nrer}(\lambda)^{d(x)}$. For a fixed object–camera distance $d(x)$, the intensity of an attenuated artificial lighting $E_\lambda^L \cdot \text{Nrer}(\lambda)^{d(x)}$ is a constant. The difference in terms of brightness perceived by a camera for fixed $d(x)$ can therefore be attributed to the reflectance of objects. Of all the pixels with the same $d(x)$, finding solutions for $E_\lambda^L$, $\rho_{\text{red}}(x)$, $\rho_{\text{green}}(x)$, and $\rho_{\text{blue}}(x)$ is an overdetermined problem and can be considered as an optimization least squares solution. In this problem, the number of equations exceeds the number of unknowns. There is generally no exact solution but an approximate solution that minimizes the quadratic error $\|((E_\lambda^A(x) \cdot \text{Nrer}(\lambda)^{D(x)} + E_\lambda^L \cdot \text{Nrer}(\lambda)^{d(x)}) \cdot \rho_\lambda(x)) - J_\lambda(x)\|^2$ [Note that the term $J_\lambda(x) = (E_\lambda^A(x) \cdot \text{Nrer}(\lambda)^{D(x)} + E_\lambda^L \cdot \text{Nrer}(\lambda)^{d(x)}) \cdot \rho_\lambda(x) = I_\lambda(x) - (1 - \text{Nrer}(\lambda)^{d(x)}) \cdot B_\lambda/\text{Nrer}(\lambda)^{d(x)}$ is known through (7)]. This approximate solution is called the least squares solution and is computed by using the pseudoinverse of $J_\lambda(x)$ as follows:

$$\rho_\lambda(x) = \left(J_\lambda(x)^T \cdot J_\lambda(x)\right)^{-1} \cdot J_\lambda(x)^T$$
$$\cdot \left(E_\lambda^A(x) \cdot \text{Nrer}(\lambda)^{D(x)} + E_\lambda^L \cdot \text{Nrer}(\lambda)^{d(x)}\right),$$
$$\lambda \in \{\text{red, green, blue}\}. \quad (19)$$

Fig. 9 shows the distribution of the luminance of an artificial light source present and the reflectance of red, green, and blue channels in Fig. 7.

After deriving the luminance contributed by the artificial light source $E_\lambda^L$ and reflectivity $\rho_\lambda(x)$, $\lambda \in \{\text{red, green, blue}\}$, at point $x$, the influence caused by the artificial lighting can be removed by subtraction from (7) as follows:

$$\hat{I}_\lambda(x) = I_\lambda(x) - \left(\left(E_\lambda^L \cdot \text{Nrer}(\lambda)^{d(x)}\right) \cdot \rho_\lambda(x)\right) \cdot \text{Nrer}(\lambda)^{d(x)}$$
$$= \left(E_\lambda^A(x) \cdot \text{Nrer}(\lambda)^{D(x)} \cdot \rho_\lambda(x)\right) \cdot \text{Nrer}(\lambda)^{d(x)}$$
$$+ \left(1 - \text{Nrer}(\lambda)^{d(x)}\right) \cdot B_\lambda, \quad \lambda \in \{\text{red, green, blue}\}. \quad (20)$$
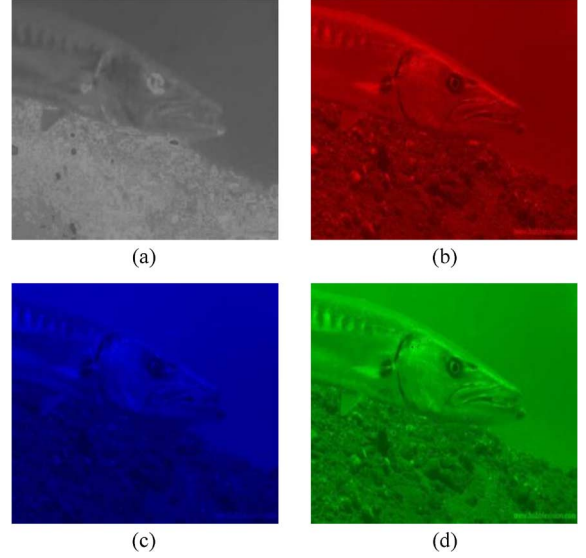


Fig. 9. Distribution of (a) the luminance of an artificial light source and (b) red, (c) green, and (d) blue channel reflectivity.
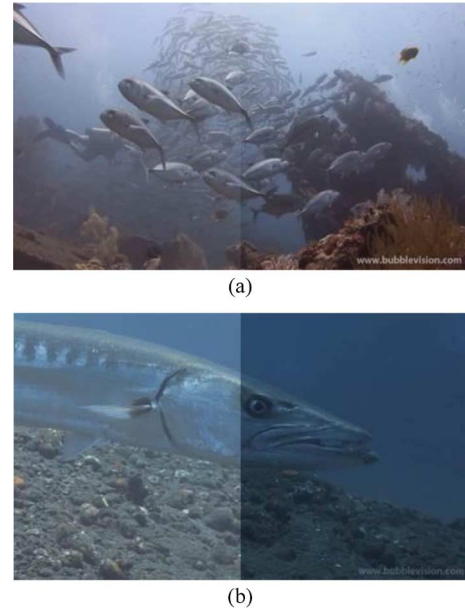


Fig. 10. Underwater image obtained after the removal of the artificial light is shown in the right panel of the split screen, whereas the original one is in the left panel. The influence of an artificial light depends on the object–camera distance. The closer the object, the more significant the impact is.

The split screens of Fig. 10(a) and (b) show the results (see right panel) after eliminating the artificial lighting detected in Figs. 1 and 7 (see left panel), respectively. Due to the size of scene area covered, the amount of artificial light received in Fig. 7 is more concentrated and larger than that of Fig. 1.

## C. Compensation of Light Scattering and Color Change Along the Object–Camera Path

After removing the artificial light source $L$ and deriving distance $d(x)$ between an object and the camera, the haze can be removed by subtracting the in-scattering term $(1 - t_\lambda(x)) \cdot B_\lambda$
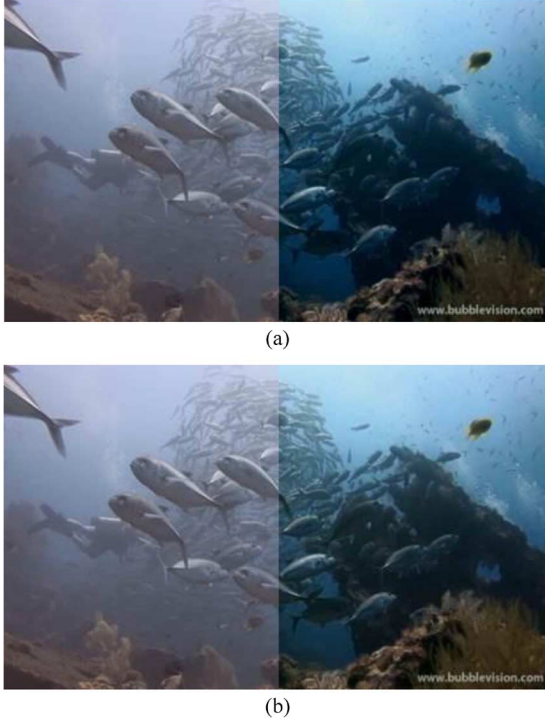
(a)



(b)

Fig. 11. Underwater image obtained (a) after eliminating haze and (b) color change along the object–camera light propagation route $d(x)$ is shown in the right panel of the split screen, respectively, whereas the original image, i.e., in Fig. 1, is in the left panel. A bluish color offset remains prevalent.

in (1) of the hazy image formation model from image $I_\lambda(x)$ perceived by the camera, i.e.,

$$
I_\lambda(x) - \left(1 - \text{Nrer}(\lambda)^{d(x)}\right) \cdot B_\lambda \\
= \left(\left(E_\lambda^A(x) \cdot \text{Nrer}(\lambda)^{D(x)}\right) \cdot \rho_\lambda(x)\right) \cdot \text{Nrer}(\lambda)^{d(x)}. \quad (21)
$$

The image after dehazing is shown in the right panel of Fig. 11(a). Next, the color change encountered during the object–camera path can be corrected by dividing both sides of (21) by the wavelength-dependent attenuation ratio $\text{Nrer}(\lambda)^{d(x)}$. Therefore, the image after the dehazing and correction of color change introduced through the propagation path $d(x)$ can be formulated as

$$
J_\lambda(x) = \frac{I_\lambda(x) - \left(1 - \text{Nrer}(\lambda)^{d(x)}\right) \cdot B_\lambda}{\text{Nrer}(\lambda)^{d(x)}} \\
= \left(E_\lambda^A(x) \cdot \text{Nrer}(\lambda)^{D(x)}\right) \cdot \rho_\lambda(x), \\
\lambda \in \{\text{red, green, blue}\}. \quad (22)
$$

The right panel of the split screen in Fig. 11(b) shows the result after the removal of light scattering and correction of color change along the object–camera path $d(x)$. A bluish color offset remains prevalent across the whole frame. This is due to the disparity in the amount of wavelength attenuation encountered when skylight penetrates through the water surface reaching the imaging scene, causing underwater environments illuminated by the bluish ambient light. The further estimation of the water depth of the image scene is required to satisfactorily correct the color change introduced along the course of propagation from the water surface to the photographic scene.



Fig. 12. Underwater image after removing light scattering and color change by considering the artificial light source $L$, the object–camera distance $d(x)$, and the depth from the water surface to top of image $D$. As the depths of the top and bottom of the image are different, visible color change distortion still exists at the lower portion of the image.

Since our goal is to obtain a haze-free and color-corrected image, $E_\lambda^A(x) \cdot \rho_\lambda(x)$. The only unknown left in (22) is the water depth $D(x)$ of point $x$. In the next subsection, the derivation of scene depth will be discussed.

### D. Underwater Depth at the Top of the Photographic Scene: $D$

For the homogeneous skylight $A$, the energy corresponding to red, green, blue channels right above the water surface shall be the same, i.e., $E_{\text{red}}^A = E_{\text{green}}^A = E_{\text{blue}}^A$. After penetrating the water depth $D$, the energy of each color channel after attenuation, i.e., the underwater ambient light $E_\lambda^w$, $\lambda \in \{\text{red, green, blue}\}$, becomes $E_{\text{red}}^w$, $E_{\text{green}}^w$, and $E_{\text{blue}}^w$, respectively. To estimate the underwater depth $D$, the corresponding intensity of the ambient lighting shall be detected first. Therefore, the water depth $D$ is the least squares solution that makes the difference between the attenuated version of the incident light $E_{\text{red}}^A$, $E_{\text{green}}^A$, and $E_{\text{blue}}^A$ after propagation, and the detected ambient lighting $E_\lambda^w$, $\lambda \in \{\text{red, green, blue}\}$ in depth $D$, with energy $E_{\text{red}}^w$, $E_{\text{green}}^w$, and $E_{\text{blue}}^w$ at the minimum as follows:

$$
\min_k \sum_\lambda \left\| \left(E_\lambda^w - E_\lambda^A \cdot (\text{Nrer}(\lambda))^k\right) \right\|^2, \\
\lambda \in \{\text{red, green, blue}\}. \quad (23)
$$

Once $D$ is determined, the amount of attenuation in each wavelength can be utilized to compensate the energy differences and correct the color change distortion by dividing (22) with $\text{Nrer}(\lambda)^D$ as follows:

$$
\hat{J}_\lambda(x) = \frac{J_\lambda(x)}{\text{Nrer}(\lambda)^D}, \quad \lambda \in \{\text{red, green, blue}\} \quad (24)
$$

where $\hat{J}_\lambda(x)$ is the restored energy of the underwater image after haze removal and calibration of color change, as shown in Fig. 12. However, the water depths at the top and bottom of the scene are usually not the same in a typical image. Employing a single value of depth $D$ to compensate the entire image will leave visible color change at the bottom portion since the intensity of incident light decreases significantly as the water depth increases. Thus, the refinement of depth estimation for each point in the image is necessary to achieve correct energy compensation at different depths.

Fig. 13. Underwater image obtained after processing with WCID. The depth of the underwater scene ranges from 5 m at the top of the image to 8 m at the bottom portion.
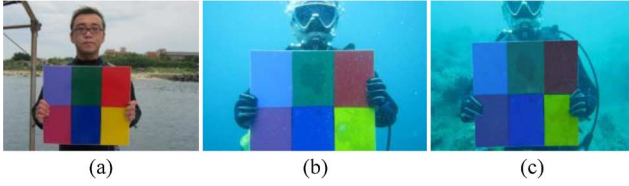


Fig. 14. Diver holding a board with six patches of designated colors, (a) before diving, diving at a depth of (b) 5 m, and (c) 15 m.

### E. Image Depth Range R

The image acquired covers a depth range of tan underwater scene from $D$ to $D + R$, as shown in Fig. 2. When light penetrates through water covering the depth range $R$, a disparate amount of color change will be induced at the top and at the bottom of the image. This phenomenon necessitates varying energy compensation adjusted according to the depth of each underwater point to correctly rectify color change.

Let the top background pixel be the point at the top of the image background with the underwater depth $D$, and let the bottom point at the bottom of the image background with the underwater depth $D + R$, where $R$ represents the range of water depth covered in an image. By detecting the corresponding intensity of background light at depths $D$ and $D + R$, the value of the shallowest water depth $D$ and the deepest water depth $D + R$ can be derived from (23). The water depth of any point $x$ in the image is between the depth range $D$ through $D + R$. Therefore, the depth of an image point can be fine-tuned by linear interpolation, i.e., that of the top and bottom background points. Suppose that pixel $x$ and top and bottom background pixels are located on scanline $a_x, b$, and $c$, respectively. The underwater depth $D(x)$ of pixel $x$ can be derived pointwise by linear interpolation as follows:

$$D(x) = D + R \cdot \frac{a_x - b}{c - b}, \quad b \leq a_x \leq c. \quad (25)$$

Once the underwater depths for all pixels are obtained, the restored energy $\hat{J}_\lambda(x)$ of the underwater image after haze removal and calibration of color change in (24) can be modified to better compensate the energy loss during light propagation along different water depths by dividing (22) with $\text{Nrer}(\lambda)^{D(x)}$ instead of $\text{Nrer}(\lambda)^D$

$$\hat{J}_\lambda(x) = \frac{J_\lambda(x)}{\text{Nrer}(\lambda)^{D(x)}}$$
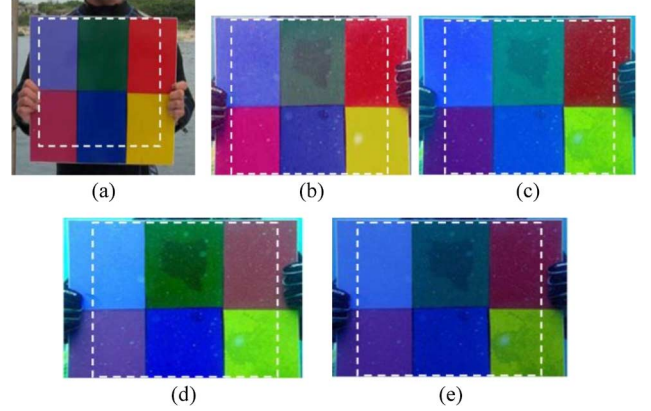$$= E_\lambda^A(x) \cdot \rho_\lambda(x), \quad \lambda \in \{\text{red, green, blue}\}. \quad (26)$$



Fig. 15. (a) The color board, serving as a ground truth, of the image taken above water in Fig. 14(a). Color boards obtained after processing Fig. 14(b) with (b) WCID, (c) dark-channel-based dehazing algorithm, (d) chromatism-based dehazing algorithm, and (e) histogram equalization. The dotted white rectangles correspond to the effective color areas for computing SNR values, as listed in Table I.

TABLE I
QUANTITATIVE PERFORMANCE EVALUATION: SNR VALUES FOR THE EFFECTIVE COLOR AREAS IN FIG. 15(b)–(e) (WATER DEPTH 5 m) AND FIG. 16(a)–(d) (WATER DEPTH 10 m) BY EMPLOYING THE EFFECTIVE COLOR AREA IN FIG. 15(a) AS THE GROUND-TRUTH IMAGE ARE LISTED

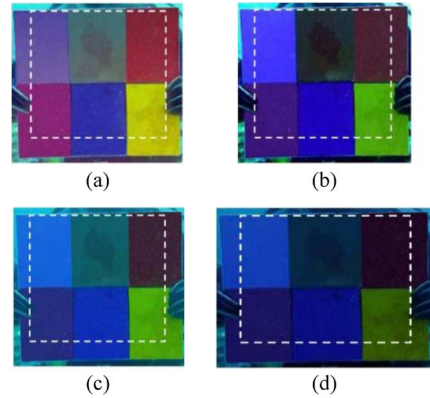|  | WCID | dark-channel dehazing | chromatism -based dehazing | histogram equalization |
|---|---|---|---|---|
| 5M | 19.72 dB | 13.29 dB | 13.39 dB | 12.50 dB |
| 15M | 18.41 dB | 10.33 dB | 11.51 dB | 5.65 dB |



Fig. 16. Color boards obtained after processing Fig. 14(c) with (a) WCID, (b) dark-channel-based dehazing algorithm, (c) chromatism-based dehazing algorithm, and (d) histogram equalization. The dotted white rectangles correspond to the effective color areas for computing SNR values, as listed in Table I.

Other than taking the artificial light source $L$, the object–camera distance $d(x)$, and the water depth $D$ into consideration, Fig. 13 demonstrates the result of fine tuning the amount of wavelength compensation by deriving the water depth $D(x)$ of every image pixel $x$, where the $\text{Nrer}(\lambda)$ values used for red, green, and blue light are 82%, 95%, and 97.5%, respectively. In comparison with Fig. 12, the color change suffered at the lower part of the image is greatly reduced. Color balance is restored for the whole image, rather than just the top portion of the frame.
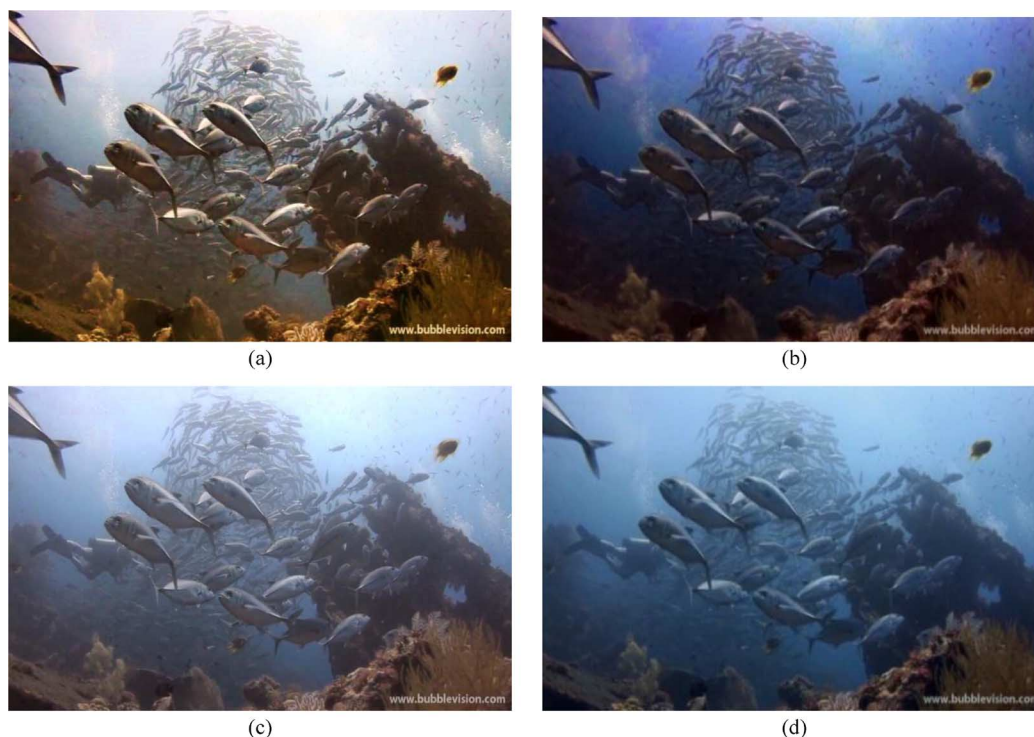
Fig. 17.   Image obtained after processing with the (a) WCID. Fig. 13 is included here for ease of comparison. (b) Dark-channel-based dehazing algorithm. (c) Chromatism-based dehazing algorithm. (d) Histogram equalization.
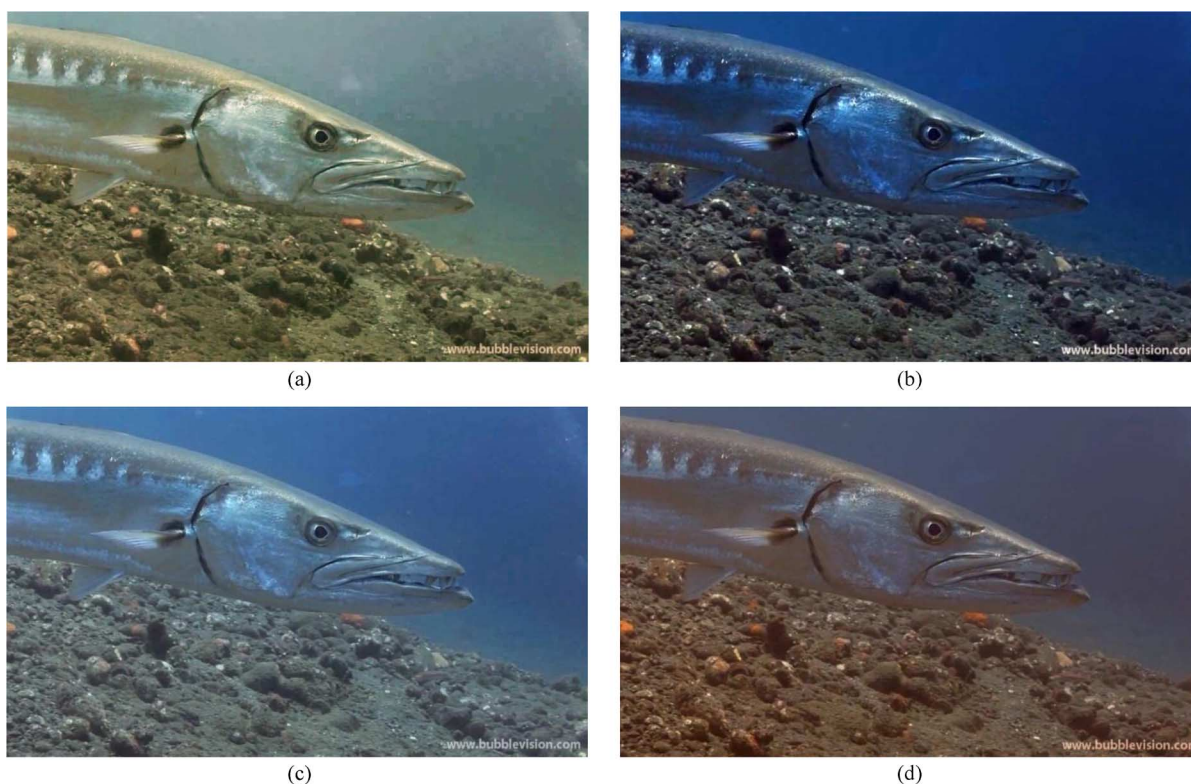


Fig. 18.   (a) Image obtained after processing with WCID. The underwater depth of the photographic scene ranges from 17 to 18 m. The brightness emitted by the artificial light source is estimated to be 100. (b) Image obtained after processing with the dark-channel-based algorithm, and (c) chromatism-based dehazing algorithm, respectively. (d) Image obtained by histogram equalization, haze effects, and color change still exist.

## III. EXPERIMENTAL RESULTS

The performance of the proposed WCID algorithm is evaluated both objectively and subjectively by utilizing ground-truth color patches and videos downloaded from Youtube website. Both results demonstrate superior haze removing and color balancing capabilities of the proposed WCID over traditional dehazing and histogram equalization methods.
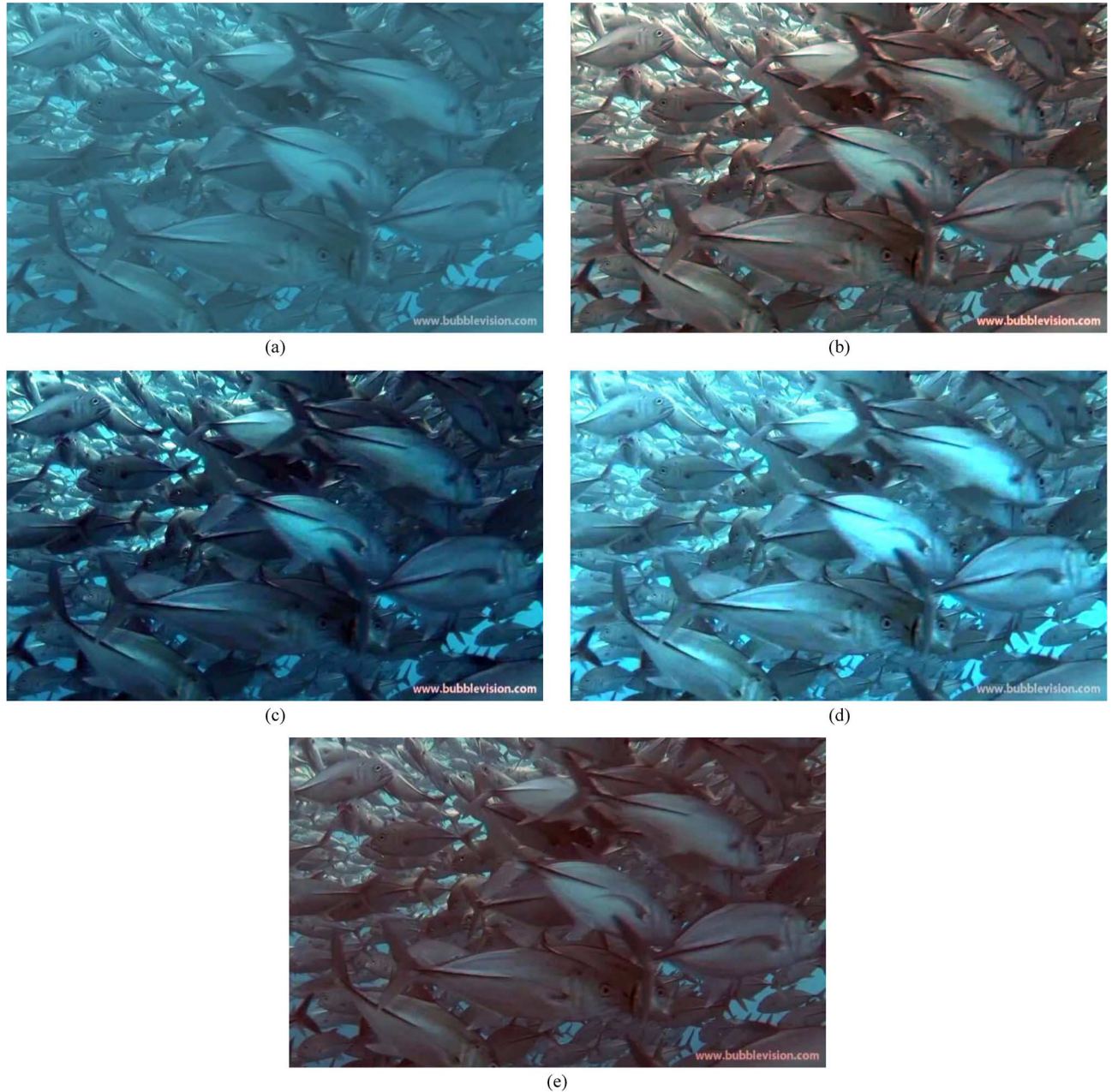
Fig. 19. (a) Underwater image extracted from the Youtube website [26]. (b) Image obtained after processing with WCID. The underwater depth of the photographic scene ranges from 18 to 22 m. (c)–(e) Image obtained after processing with dark-channel-based and chromatism-based dehazing algorithms and histogram equalization, respectively.

## A. Objective Performance Evaluation

Pictures taken for a diver holding a board with six patches of designated colors before diving (ground truth), and diving at a depth of 5 and 15 m, respectively, are shown in Fig. 14(a)–(c). The colors processed by the WCID proposed, by dark-channel dehazing [8], by chromatism-based dehazing [24], and histogram equalization algorithms [11] are compared with the ground-truth ones taken above water, as shown in Figs. 15(a)–(e) and 16(a)–;(d). Due to the difficulty in maintaining a consistent spatial relationship between the color board and the camera, size and orientation variances exist between pictures taken underwater. In calculating the SNR values, the size and orientation of the color board are first adjusted to match those of the ground-truth image. The areas occluded by the diver's fingers and the lower portion of the color board, which is not within the scope of the image taken in Fig. 14(b), are exluded. The dotted white rectangles in Figs. 15 and 16 correspond to the effective color areas employed in deriving the SNR values. As shown in Table I, the WCID proposed obtains the highest SNR value in both depths. In addition, the performance of WCID is the most robust through different water depths due to the incorporation of wavelength compensation, image dehazing, and artificial lighting removal. On the other hand, the SNR value obtained by histogram equalization drops significantly as the depth increases. This is due to the fact that the dynamic range of the red color component decreases substantially with the depth due to wavelength attenuation. An

Fig. 20.   (a) Underwater shipwreck image extracted from the Youtube website [27]. (b) Image obtained after processing with WCID. The underwater depth of the photographic scene ranges from 3 to 8 m. (c)–(e) Image obtained after processing with dark-channel-based and chromatism-based dehazing algorithms and histogram equalization, respectively.

attempt, without taking dehazing or wavelength compensation into consideration, blindly expanding the range of color components will adversely accompany with a huge amount of error. The relatively low value of the SNR can be attributed to the presence of water bubbles, the misalignment in matching color patches with different dimensions and orientations, and water permeated through the seam between the green color patch and the board, making it distinct from the counterpart in the ground-truth image.

### B. Subjective Performance Evaluation

Fig. 1 is extracted from an underwater video on the Youtube website filmed by the Bubble Vision Company. [26]. This AVI-formatted video is 350 s long with a resolution of 720p. Fig. 17(b) and (c) shows the result after processing with a

dark-channel-based algorithm and a chromatism-based dehazing algorithm, respectively. Although the contrast of the image is increased, the color change appears even more prominent as the attenuated energy is not compensated individually based on different wavelengths. Fig. 17(d) illustrates the image after histogram equlaization processing, from which the haze effect and color change still remain. In comparison with results processed by these conventional techniques, the image processed by the WCID method, as shown in Fig. 13, is effectively haze free and color balanced. We give the image the original color and clarity that it would have had if it were not taken underwater.

Fig. 7 is another image from the same video sequence used to demonstrate the effect of the presence of a strong artificial light source. The result after WCID processing, i.e., Fig. 18(a),
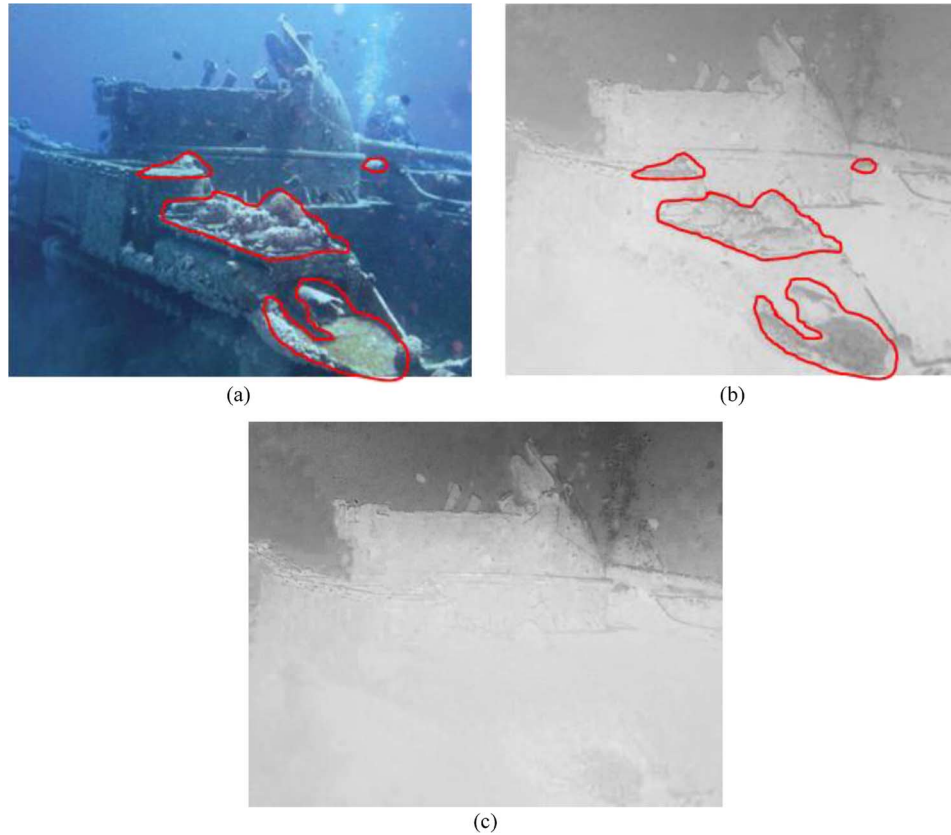
Fig. 21. (a) Relatively large white shiny regions are marked by the red lines. (b) The marked regions are mistakenly classified as background by the dark-channel prior. (c) Depth map refinement through graph-cut-based $\alpha$-expansion. Most of the misjudged areas are corrected.

is superior to those by the dehazing algorithms or histogram equalization, as shown in Fig. 18(b)–(d), in terms of both color balance and clarity.

Two more sets of test images and processing results are shown in Figs. 19 and 20 to facilitate further comparison. Fig. 19(a) is included for its variety in terms of subjects' scene depth, encompassing close to far range, whereas Fig. 20(a) is included for the uniqueness of subject, i.e., a shipwreck, on the sea floor. A consistent dehazing effect and color balance are obtained throught the processing of the WCID proposed. More test videos can be downloaded from ftp://140.117.168.28.

## IV. CONCLUSION

The WCID algorithm proposed in this paper can effectively restore image color balance and remove haze. To the best of our knowledge, no existing techniques can handle light scattering and color change distortions suffered by underwater images simultaneously. The experimental results demonstrate superior haze removing and color balancing capabilities of the proposed WCID over traditional dehazing and histogram equalization methods. However, the salinity and the amount of suspended particles in ocean water vary with time, location, and season, making accurate measurement of the rate of light energy loss Nrer$(\lambda)$ difficult. Errors in the rate of light energy loss will affect the precision of both the water depth $D(x)$ and the underwater propagation distance $d(x)$ derived. Constant monitoring and long-term tabulation of the rate of light energy loss according to time, location, and season might provide a

reasonable estimate of the actual value. In addition, a calibration procedure might be performed first by drivers before an image-capturing session by taking a test picture at known water depth and underwater propagation distance to fine-tune the rate of light energy loss. In addition, the artificial lighting $L$ is assumed to be a point source emitting uniform omnidirectional light beams across all wavelength spectrums. This is different from the linear or surface light source with a strong beam directionality and nonuniform color characteristic commonly encountered in underwater photography. The precise estimation of the luminance distribution of the light source is also demanding. If the geographic location in taking the underwater footage and the characteristics of the light source employed are known *a priori*, even better results in haze removal and color balance can be reached.

Another source for causing compensation errors is the estimation of the scene depth $d(x)$ by the dark-channel prior, as commonly encountered in depth derivation by utilizing a single image. Relatively large white shiny regions of a foreground object might be misjudged as far away ones. For example, in Fig. 21(a), the area marked by red lines are mistaken as background, as shown in Fig. 21(b). Two approaches are suggested to alleviate the above situation [25]. One is enlarging the size of the local patch $\Omega(x)$ formulated in (9). Another is depth refinement by utilizing spatial and temporal correlation within and between video frames. The depth map refined through the graph-cut-based $\alpha$-expansion method [25] is shown in Fig. 21(c).

APPENDIX A

In order to show the validity of the inequality shown in the first equation at the bottom of the page, supports from the following two lemmas are needed.

*Lemma 1:*

$$\min_{\lambda}\left(\frac{A_\lambda}{B_\lambda}\right) \leq \frac{\min_\lambda A_\lambda}{\min_\lambda B_\lambda}, \forall A_\lambda, B_\lambda > 0, \lambda \in \{\text{red, green, blue}\}.$$

*Proof:* Let

$$A_\lambda = \min_{y \in \Omega(x)}\left(\left(E_\lambda^A(y) \cdot \text{Nrer}(\lambda)^{D(y)} + E_\lambda^L \cdot \text{Nrer}(\lambda)^{d(x)}\right)\right.$$
$$\left. \cdot \rho_\lambda(y)\right) \cdot \text{Nrer}(\lambda)^{d(x)}, \lambda \in \{\text{red, green, blue}\}.$$

According to the law of physics, the normalized residual energy ratio Nrer(red) < Nrer(green) < Nrer(blue). The following inequality for ambient light $B_\lambda$ can be established in an underwater environment as follows:

$$B_{\text{red}} < B_{\text{green}} < B_{\text{blue}}.$$

This implies that $\min_\lambda B_\lambda = B_{\text{red}}$ and that $\max_\lambda B_\lambda = B_{\text{blue}}$.

Then

$$\min_{\lambda}\left(\frac{A_\lambda}{B_\lambda}\right) \approx \min_{\lambda}\left(\frac{A_\lambda}{B_{\text{blue}}}\right) = \frac{\min_\lambda A_\lambda}{B_{\text{blue}}} < \frac{\min_\lambda A_\lambda}{B_{\text{red}}}$$
$$= \frac{\min_\lambda A_\lambda}{\min_\lambda B_\lambda}.$$

Following this line of thought, we obtain the second equation at the bottom of the page.

Next, we want to show the numerator at the right-hand side of the above equation can be further represented as an alternative form as shown in the third equation at the bottom of the page.

*Lemma 2:*

$$\min_{\lambda}(A_\lambda \cdot C_\lambda) \approx \min_{\lambda} A_\lambda \cdot \min_{\lambda} C_\lambda, \forall A_\lambda, C_\lambda > 0,$$
$$\lambda \in \{\text{red, green, blue}\}.$$

*Proof:* Let

$$A_\lambda = \min_{y \in \Omega(x)}\left(\left(E_\lambda^A(y) \cdot \text{Nrer}(\lambda)^{D(y)} + E_\lambda^L \cdot \text{Nrer}(\lambda)^{d(x)}\right)\right.$$
$$\left. \cdot \rho_\lambda(y)\right), \quad \lambda \in \{\text{red, green, blue}\}.$$
$$C_\lambda = \text{Nrer}(\lambda)^{d(x)}, \quad \lambda \in \{\text{red, green, blue}\}.$$

According to the normalized residual energy ratio Nrer(red) < Nrer(green) < Nrer(blue), the inequality for $C_\lambda$ is as follows:

$$C_{\text{red}} < C_{\text{green}} < C_{\text{blue}}.$$

Then

$$\min_{\lambda}(A_\lambda C_\lambda) \approx \min_{\lambda}(A_\lambda C_{\text{red}}) = C_{\text{red}} \min_{\lambda}(A_\lambda)$$
$$= \min_{\lambda}(C_\lambda) \min_{\lambda}(A_\lambda).$$

---

$$\min_{\lambda}\left\{\frac{\min\limits_{y \in \Omega(x)}\left(\left(E_\lambda^A(y) \cdot \text{Nrer}(\lambda)^{D(y)} + E_\lambda^L \cdot \text{Nrer}(\lambda)^{d(x)}\right) \cdot \rho_\lambda(y)\right)}{B_\lambda} \cdot \text{Nrer}(\lambda)^{d(x)}\right\}$$
$$\leq \frac{\min\limits_{\lambda}\left(\min\limits_{y \in \Omega(x)}\left(\left(E_\lambda^A(y) \cdot \text{Nrer}(\lambda)^{D(y)} + E_\lambda^L \cdot \text{Nrer}(\lambda)^{d(x)}\right) \cdot \rho_\lambda(y)\right)\right) \cdot \min\limits_{\lambda}\left(\text{Nrer}(\lambda)^{d(x)}\right)}{\min\limits_{\lambda}(B_\lambda)}$$

---

$$\min_{\lambda}\left\{\frac{\min\limits_{y \in \Omega(x)}\left(\left(E_\lambda^A(y) \cdot \text{Nrer}(\lambda)^{D(y)} + E_\lambda^L \cdot \text{Nrer}(\lambda)^{d(x)}\right) \cdot \rho_\lambda(y)\right)}{B_\lambda} \cdot \text{Nrer}(\lambda)^{d(x)}\right\}$$
$$\leq \frac{\min\limits_{\lambda}\left\{\min\limits_{y \in \Omega(x)}\left(\left(E_\lambda^A(y) \cdot \text{Nrer}(\lambda)^{D(y)} + E_\lambda^L \cdot \text{Nrer}(\lambda)^{d(x)}\right) \cdot \rho_\lambda(y)\right) \cdot \text{Nrer}(\lambda)^{d(x)}\right\}}{\min\limits_{\lambda} B_\lambda}.$$

---

$$\min_{\lambda}\left\{\min\limits_{y \in \Omega(x)}\left(\left(E_\lambda^A(y) \cdot \text{Nrer}(\lambda)^{D(y)} + E_\lambda^L \cdot \text{Nrer}(\lambda)^{d(x)}\right) \cdot \rho_\lambda(y)\right) \cdot \text{Nrer}(\lambda)^{d(x)}\right\}$$
$$\approx \min_{\lambda} \min_{y \in \Omega(x)}\left(\left(E_\lambda^A(y) \cdot \text{Nrer}(\lambda)^{D(y)} + E_\lambda^L \cdot \text{Nrer}(\lambda)^{d(x)}\right) \cdot \rho_\lambda(y)\right) \cdot \min_{\lambda} \text{Nrer}(\lambda)^{d(x)}.$$

Therefore

$$
\min_{\lambda} \left\{ \min_{y \in \Omega(x)} \left( \left( E_\lambda^A(y) \cdot \mathrm{Nrer}(\lambda)^{D(y)} + E_\lambda^L \cdot \mathrm{Nrer}(\lambda)^{d(x)} \right) \right. \right.
$$
$$
\left. \left. \cdot \rho_\lambda(y) \right) \cdot \mathrm{Nrer}(\lambda)^{d(x)} \right\}
$$
$$
\approx \min_{\lambda} \min_{y \in \Omega(x)} \left( \left( E_\lambda^A(y) \cdot \mathrm{Nrer}(\lambda)^{D(y)} + E_\lambda^L \cdot \mathrm{Nrer}(\lambda)^{d(x)} \right) \right.
$$
$$
\left. \cdot \rho_\lambda(y) \right) \cdot \min_{\lambda} \mathrm{Nrer}(\lambda)^{d(x)}.
$$

### REFERENCES

[1] K. Lebart, C. Smith, E. Trucco, and D. M. Lane, "Automatic indexing of underwater survey video: algorithm and benchmarking method," *IEEE J. Ocean. Eng.*, vol. 28, no. 4, pp. 673–686, Oct. 2003.

[2] J. Yuh and M. West, "Underwater robotics," *Adv. Robot.*, vol. 15, no. 5, pp. 609–639, 2001.

[3] J. R. Zaneveld and W. Pegau, "Robust underwater visibility parameter," *Opt. Exp.*, vol. 11, no. 23, pp. 2997–3009, 2003.

[4] E. Trucco and A. T. Olmos-Antillon, "Self-tuning underwater image restoration," *IEEE J. Ocean. Eng.*, vol. 31, no. 2, pp. 511–519, Apr. 2006.

[5] J. S. Jaffe, "Computer modeling and the design of optimal underwater imaging systems," *IEEE J. Ocean. Eng.*, vol. 15, no. 2, pp. 101–111, Apr. 1990.

[6] M. C. W. van Rossum and T. M. Nieuwenhuizen, "Multiple scattering of classical waves: Microscopy, mesoscopy and diffusion," *Rev. Modern Phys.*, vol. 71, no. 1, pp. 313–371, Jan. 1999.

[7] Y. Y. Schechner and N. Karpel, "Recovery of underwater visibility and structure by polarization analysis," *IEEE J. Ocean. Eng.*, vol. 30, no. 3, pp. 570–587, Jul. 2005.

[8] L. Chao and M. Wang, "Removal of water scattering," in *Proc. Int. Conf. Comput. Eng. Technol.*, 2010, vol. 2, pp. 35–39.

[9] W. Hou, D. J. Gray, A. D. Weidemann, G. R. Fournier, and J. L. Forand, "Automated underwater image restoration and retrieval of related optical properties," in *Proc. IGARSS*, 2007, vol. 1, pp. 1889–1892.

[10] A. Yamashita, M. Fujii, and T. Kaneko, "Color registration of underwater image for underwater sensing with consideration of light attenuation," in *Proc. Int. Conf. Robot. Autom.*, 2007, pp. 4570–4575.

[11] K. Iqbal, R. Abdul Salam, A. Osman, and A. Zawawi Talib, "Underwater image enhancement using an integrated color model," *Int. J. Comput. Sci.*, vol. 34, no. 2, pp. 2–12, 2007.

[12] I. Vasilescu, C. Detwiler, and D. Rus, "Color-accurate underwater imaging using perceptual adaptive illumination," in *Proc. Robot. Sci. Syst.*, Zaragoza, Spain, 2010.

[13] K. He, J. Sun, and X. Tang, "Single image haze removal using Dark Channel Prior," in *Proc. IEEE CVPR*, 2009, vol. 1, pp. 1956–1963.

[14] S. Shwartz, E. Namer, and Y. Y. Schechner, "Blind haze separation," in *Proc. IEEE CVPR*, 2006, vol. 2, pp. 1984–1991.

[15] J. T. Houghton, *The Physics of Atmospheres*, 2nd ed. Cambridge, U.K.: Cambridge Univ. Press, 2001, ch. 2.

[16] W. N. McFarland, "Light in the sea—Correlations with behaviors of fishes and invertebrates," *Amer. Sci. Zoology*, vol. 26, no. 2, pp. 389–401, 1986.

[17] S. Q. Duntley, "Light in the sea," *J. Opt. Soc. Amer.*, vol. 53, no. 2, pp. 214–233, 1963.

[18] L. A. Torres-Méndez and G. Dudek, "Color correction of underwater images for aquatic robot inspection," in *Proc. EMMCVPR*, 2005, vol. 3757, Lecture Notes in Computer Science, pp. 60–73.

[19] N. G. Jerlov, *Optical Oceanography*. Amsterdam, The Netherlands: Elsevier, 1968.

[20] R. Tan, "Visibility in bad weather from a single image," in *Proc. IEEE CVPR*, 2008, vol. 1, pp. 1–8.

[21] R. Fattal, "Single image dehazing," in *Proc. Int. Conf. Comput. Graph. Interact. Tech.*, 2008, pp. 1–9.

[22] A. Levin, D. Lischinski, and Y. Weiss, "A closed form solution to natural image matting," in *Proc. IEEE CVPR*, 2006, vol. 1, pp. 61–68.

[23] Y. Y. Schechner and N. Karpel, "Clean Underwater Vision," in *Proc. IEEE CVPR*, 2004, vol. 1, pp. 536–543.

[24] N. Carlevaris-Bianco, A. Mohan, and R. M. Eustice, "Initial results in underwater single image dehazing," in *Proc. IEEE OCEANS*, 2010, pp. 1–8.

[25] C. Perer and H. Richard, "Improved Single Image Dehazing Using Geometry," in *Proc. IEEE DICTA*, 2009, pp. 103–110.

[26] [Online]. Available: http://www.youtube.com/user/bubblevision.

[27] [Online]. Available: http://www.youtube.com/watch?v=NKmc5dlVSRk&hd=1

**John Y. Chiang** received the B.S. degree in electrical engineering from National Taiwan University, Taipei, Taiwan, in 1985, and the M.S. and Ph.D. degrees in electrical engineering from the Northwestern University, Evanston, IL, in 1987 and 1990, respectively.

He is currently an Associate Professor with the Department of Computer Science and Engineering, National Sun Yat-Sen University, Kaohsiung, Taiwan. His research interests include image processing, computerized tongue diagnosis in traditional Chinese medicine, and content-based image retrieval.

**Ying-Ching Chen** received the B.S. degree in information engineering from I-Shou University, Kaohsiung, Taiwan, in 2009 and the M.S. degree from National Sun Yat-Sen University, Kaohsiung, in 2011.

He is currently fulfilling his one-year mandatory military service. His research interests include image processing and pattern recognition.